Earthq Eng & Eng Vib (2020) 19: 919-935 **DOI**: https://doi.org/10.1007/s11803-020-0604-8

Model test and numerical simulation on the dynamic stability of the bedding rock slope under frequent microseisms

Deng Zhiyun[1,2†], Liu Xinrong[1,2‡], Liu Yongquan[1,2,3†], Liu Shulin[1,2§], Han Yafeng[1,2†], Liu Jinhui[1,2§] and Tu Yiliang[4†]

1. *School of Civil Engineering, Chongqing University, Chongqing 400045, China*
2. *National Joint Engineering Research Center for Prevention and Control of Environmental Geological Hazards in the TGR Area Chongqing University, Chongqing 400045, China*
3. *China Construction Underground Space Co., Ltd., Chengdu 610081, China*
4. *School of civil engineering, Chongqing Jiaotong University, Chongqing 400074, China*

Abstract: Shake table testing was performed to investigate the dynamic stability of a mid-dip bedding rock slope under frequent earthquakes. Then, numerical modelling was established to further study the slope dynamic stability under purely microseisms and the influence of five factors, including seismic amplitude, slope height, slope angle, strata inclination and strata thickness, were considered. The experimental results show that the natural frequency of the slope decreases and damping ratio increases as the earthquake loading times increase. The dynamic strength reduction method is adopted for the stability evaluation of the bedding rock slope in numerical simulation, and the slope stability decreases with the increase of seismic amplitude, increase of slope height, reduction of strata thickness and increase of slope angle. The failure mode of a mid-dip bedding rock slope in the shaking table test is integral slipping along the bedding surface with dipping tensile cracks at the slope rear edge going through the bedding surfaces. In the numerical simulation, the long-term stability of a mid-dip bedding slope is worst under frequent microseisms and the slope is at risk of integral sliding instability, whereas the slope rock mass is more broken than shown in the shaking table test. The research results are of practical significance to better understand the formation mechanism of reservoir landslides and prevent future landslide disasters.

Keywords: bedding rock slope; frequent microseisms; shaking table test; numerical simulation; dynamic stability; failure mode; long-term stability

1 Introduction

Seismically induced failure of rock slopes is one of the most common geological hazards in mountainous regions. Landslides may cause severe traffic interruption, structural destruction and the loss of human life (Tang *et al.*, 2009; Zhang *et al.*, 2010; Liu *et al.*, 2014; Tang *et al.*, 2017). Consequently, the seismic stability of slopes under earthquake actions is one of the most considerable engineering problems in earthquake engineering (Lak *et al.*, 2017; Huang *et al.*, 2018; Liu *et al.*, 2019). Numerical simulation and geotechnical experience from multiple research studies show that the geological structure of a slope has a significant influence on the failure pattern in a rock slope under seismic load (Aurelian *et al.*, 2009; Koukouvelas *et al.,* 2015; Almaz and Havenith 2016), so the geological structure of a slope should be carefully considered. Under the action of earthquake and other dynamic loads, the bedding rock mass may be destroyed along a certain bedding surface, which is generally exposed in the slope surface and becomes a potential sliding surface, leading to the slope instability (Liu *et al.*, 2017). Therefore, it is of significant importance to study the dynamic stability of bedding rock slope in earthquake-prone areas.

Studies related to the dynamic stability of bedding rock slope are mostly focused on their performance under strong earthquakes (e.g., Aydan *et al.*, 2010; Barbero and Barla, 2010; Yang *et al.*, 2012; Yang *et al.*, 2014; Chen *et al.*, 2016; Fan *et al.*, 2016; Li *et al.*, 2017; Xiong and Huang, 2017; Zaei and Rao, 2017; Gibson *et al.*, 2018; Song *et al.*, 2018). However, reservoir-induced earthquakes that occur in the Three Gorges Reservoir (TGR) area are microseisms with limited strength, and

Correspondence to: Liu Xinrong, School of Civil Engineering, Chongqing University, Chongqing 400045, China
Tel: +86-23-65120727; Fax: +86-23-65120728
E-mail: liuxrong@126.com
†PhD Student ; ‡Professor; §Graduate Student

Supported by: National Natural Science Foundation of China under Grant No. 41372356, the Basic Research and Frontier Exploration Project of Chongqing, China under Grant No. cstc2018jcyjA1597, the College Cultivation Project of the National Natural Science Foundation of China under Grant No. 2018PY30 and the Graduate Scientific Research and Innovation Foundation of Chongqing, China under Grant No. CYS18026
Received June 25, 2018; **Accepted** April 2, 2019

are characterized by high frequency, weak magnitude, shallow hypocenter, and rapid energy attenuation (Li and Huang, 2008). A single microseism has a minor effect on slope stability, so there is limited research concerning the performance of slopes under the microseisms. However, Napier *et al.* (1997) pointed out that repeated frequent microseisms might cause dynamic fatigue instability of slopes by the accumulation of frequent damage of rock masses. Thus, the effect of microseisms on the long-term stability of slopes should not be ignored. Studies on the dynamic stability under microseisms have also been recently performed.

Shaking table tests are often used as the most immediate way to simulate the variation of dynamic response and reveal the failure modes of rock slopes under seismic excitation (Yang *et al.*, 2012; Liu *et al.*, 2014; Chen *et al.*, 2016; Fan *et al.*, 2016; Li *et al.*, 2017; Deng *et al.*, 2020). Liu *et al.* (2018a) analyzed the deformation process and dynamic response of slopes with horizontal soft and hard interbeddings under repeated microseisms by shake table testing. Frequent earthquake actions were simulated by nearly 2000 times of horizontal seismic loading and the results showed that damage accumulated continuously as the loading times increased. However, strong earthquakes were adopted in the late loading phase due to testing apparatus and cost restrictions, so the final failure mode of the model slope in the shaking table test had the characteristics of the strong earthquake. In addition, it is difficult to acquire the evaluation index of slope stability directly by shaking model test. As the stability of rock slopes subjected to seismic effects can be analyzed using appropriate numerical techniques, Li *et al.* (2016) used FLAC3D to analyze the slope's dynamic stability characteristics and failure mechanism. Numerical results showed that the safety factor of the slope under micro earthquake action decreases gradually as the number of micro earthquake occurrences increases. Liu *et al.* (2018b) also adopted FLAC3D to analyze the slope stability during an earthquake and the long-term stability of the slope subjected to frequent microseisms. The results indicated that the influence of frequent microseisms on the long-term stability of the slope could not be ignored. However, opening of the structural plane will occur when the slope rock mass damage accumulates to a certain degree, which cannot be accurately reflected by FLAC3D or other continuum methods. Thus, the analytical model, which can reflect the behavior of a structural plane in the slope to open, extend and run through, should be established to study the actual behavior of slope under dynamic loads. Indeed, the discrete element method (DEM) can precisely meet the needs of the research. Liu *et al.* (2014) pointed out that the DEM has been commonly used in dynamic stability evaluation of rock slopes. The most popular representation of DEM is the commercial distinct element code of UDEC (Itasca, 2014). Liu *et al.* (2004) simulated the dynamic response of a rock slope in China under explosion using UDEC, and found the simulated results agreed well with site measurements. The results showed that the use of UDEC to simulate the dynamic response of jointed rock slopes was feasible. Bhasin and Kaynia (2004) analyzed static and dynamic rock slope stability of a 700-m-high rock slope in western Norway using UDEC. The numerical studies provided some useful insights into the deformation mechanisms of the rock slope. Kveldsvik *et al.* (2009) analyzed the seismic stability of the 800 m high Åknes rock slope by using the distinct element code UDEC, and the results indicate that an earthquake with a return period of 1000 years is likely to trigger sliding to great depth in the slope at the present ground water conditions and that the slope will be stable if it is drained. Lin *et al.* (2012) studied the mechanism of the collapse analysis of a jointed rock slope based on UDEC software and practical seismic load. Through the comparison and analysis of the actual damage of the slope body and the simulation results, it was shown that the use of the UDEC software in the collapse analysis of the crack development of a rock slope was feasible. Similar works using UDEC were carried out by Pal *et al.* (2012) and Kundu *et al.* (2017), and others. Although these studies using UDEC mainly focused on the performance of slopes under strong dynamic loads and rarely involved slopes under microseisms, they successfully demonstrated the use of UDEC in simulating the dynamic response of rock slopes.

In this study, shake table testing was performed to investigate the dynamic response and failure mode of the bedding rock slope under frequent earthquakes. Numerical modelling was then performed to further study the slope dynamic stability under purely microseisms and the influence of five factors, including seismic amplitude, slope height, slope angle, strata inclination and strata thickness, on the dynamic stability was considered. The results are useful to better understand the behavior of slope stability affected by frequent microseisms; meanwhile, it is also of practical significance in the prevention of earthquake-induced landslide disasters in reservoir areas.

2 Shaking table model test

2.1 Design of shaking table model test

2.1.1 Model preparation

The model simulated the lithology and structure of slopes in the TGR area. There was no corresponding prototype slope in terms of geometry. However, when designing the similarity relationship of slopes, large geometric similarity coefficients should be obtained to simulate large prototype slopes. The similar relation between the prototype and model system was established according to the similarity theory. Fifty parameters were considered in the shaking table test, three of which (i.e., density, elastic modulus and time) were chosen

as control variables with similarity coefficient C_ρ=1, C_E=32.6, C_t=4, respectively. Relevant parameters are listed in Table 1.

The slide-prone strata in the TGR area are mainly exposed Jurassic and Triassic sedimentary rocks. The Jurassic strata are mainly sandy mudstone, sandstone and carbonaceous shale, and the Triassic strata mainly include limestone, dolomite, marl and mixed sand shale. Dong *et al.* (2010) pointed out that the mass occurrence zone of landslide and slope collapse in the TGR area is the widely distributed slopes formed by sandstones, mudstones or the interbedding of sandstone and mudstone. Therefore, sandstone from the TGR area was taken as the material for the prototype slope. Its physical-mechanical parameters were extracted from the published literature (Jiang, 2012; Yang, 2014). According to the similarity relationship of physical quantities (shown in Table 1), the range of values of the physical-mechanical parameters for model slope can be obtained, as tabulated in Table 2.

The test samples of the model slope were made up of similar materials, which were formed of quartz sand, barite powder, gypsum, water and glycerin. It is critical to select the proper proportion of similar materials to simulate prototype slopes with greater accuracy. Based on the studies of Liu *et al.* (2011; 2012), the optimal proportion of similar materials were determined by conducting a large number of routine laboratory tests. The physico-mechanical parameters of model slope and prototype slope and the corresponding proportion of similar materials are shown in Table 3.

As the TGR area is characterized by steep topography and deep incised river valleys (Sun *et al.*, 2017), the model slope angle was set at 60°. The bottom surface of the model slope was 93 cm × 40 cm in size and the height of the model slope was 85 cm due to the limitation of the bearing capacity of the vibrating table. This design was equivalent to a prototype slope with a height of 19.4 m according to the similarity coefficient. During the test, the absorber, which was made of a foam cushion, was placed on two lateral sides of the rigid box to minimize the boundary effects on the seismic wave input. The generalized model with embedded accelerometers and the side view of the test model are shown in Figs. 1(a), 1(b).

Table 1 Similarity ratios of the test model

Parameters	Dimension analysis	Similarity ratio	Parameters	Dimension analysis	Similarity ratio
Density (ρ)	ML^{-3}	C_ρ*=1	Displacement (u)	L	$C_u=C_l C_\varepsilon$=16
Elastic modulus (E)	$ML^{-1}T^{-2}$	C_E*=32.6	Time (t)	T	C_t*=4
Poisson's ratio(μ)	-	C_μ=1	Frequency (f)	T^{-1}	$C_f=C_t^{-1}$=0.25
Cohesion (c)	$ML^{-1}T^{-2}$	$C_c=C_E C_\varepsilon$=22.8	Velocity (v)	LT^{-1}	$C_v=C_u C_t^{-1}$=4
Internal friction angle (φ)	-	C_φ=1	Acceleration (a)	LT^{-2}	$C_a=C_u C_t^{-2}$=1
Stress (σ)	$ML^{-1}T^{-2}$	$C_\sigma=C_E C_\varepsilon$=22.8	Gravitational acceleration (g)	LT^{-2}	$C_a=C_u C_t^{-2}$=1
Strain (ε)	-	$C_\varepsilon=C_\rho C_g C_l C_E^{-1}$=0.7	Damping ratio (λ)	-	C_λ=1
Length (l)	L	$C_l=C_E^{0.5} C_\rho^{-0.5} C_t$=22.8			

Note: "–" indicates the dimensionless parameters.

Table 2 Range values of physico-mechanical parameters of materials for prototype and model slope

Category	Density (g·cm^{-3})	Elastic modulus (MPa)	Poisson ratio (μ)	Cohesion (kPa)	Internal friction angle (◦)	Uniaxial compressive strength (MPa)
Prototype slope	2.0–2.5	1500–40000	0.18–0.3	2000–10000	30–45	30–70
Model slope	2.0–2.5	46–1227	0.18–0.3	88–439	30–45	1.3–3.1

Table 3 Physico-mechanical parameters of model slope and prototype slope and the proportion of similar materials

Category	Density (g·cm^{-3})	Elastic modulus (MPa)	Poisson ratio (μ)	Cohesion (kPa)	Internal friction angle (◦)	Uniaxial compressive strength (MPa)
Model slope	2.50	180	0.25	120	42	1.4
prototype slope	2.50	5868	0.25	2736	42	31.9
Proportion of similar materials	Quartz sand: barite powder: gypsum: water: glycerin=1.00: 0.60: 0.33: 0.20: 0.03					

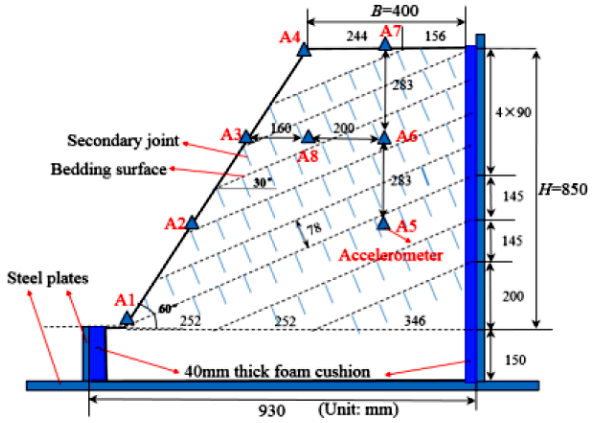

(a) Generalized model with the embedded accelerometers

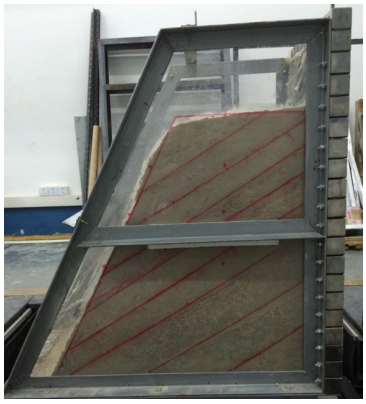

(b) Final model after production

Fig. 1 Model of slope with zigzag asperities

In Fig. 1(a), eight accelerometers were fixed on the slope model, three of which were embedded inside the slope and the others were fixed on the slope surface. Because joints are widely distributed in natural rocks, and the existence of them significantly deteriorates the deformability behavior and strength of rock masses (Liu *et al.*, 2019), bedding planes and the orthogonal secondary joints were both considered in the model slope. The spacing of the secondary joints is equal to the thickness of the rock layer and the cutting depth h was equal to 2/3 of the thickness of the rock layer. The model slope was built in the model box and compacted layer by layer from the bottom to the top. First, the required materials for each layer were identified, mixed and shoveled into the model box. Second, a made rammer was used to compact the wet-stirred material and the orthogonal secondary joints were cut. Third, a thin layer of quartz sand was evenly spread on the bedding plane after each layer was compacted. The accelerometers embedded in the slope interior were buried during the construction of the slope, and the accelerometers embedded on the slope surface were installed after the slope was completed. These steps were repeated until the slope model reached the designed height. The final model is shown in Fig. 1(b).

2.1.2 Test loading scheme

An artificial wave and a natural wave supplemented with white noise excitations (WN) were applied in the shaking table test. The natural wave adopted in this test is the earthquake record monitored by a seismological monitoring station in the Xingshan County in Hubei Province, selected as a typical reservoir-induced earthquake in the TGR area. The focal depth of the natural wave is approximately 5 km and the time of the main shock is approximately 7 s. Jiang (2012) found that the reservoir-induced earthquakes show successive characteristics that occur two to three times in a relatively short period of time (1–3 days), and it was difficult to divide them into foreshock, main shock, and aftershock type due to their similar magnitude and intensity. Therefore, the natural seismic wave applied in the experiment was taken as follows: the main shocks of four natural waves of 7 s were intercepted and spliced together as a complete seismic wave sequence and it was then compressed according to the time similarity coefficient (C_t = 4). The reservoir-induced earthquakes were mostly microseisms with a magnitude of less than 2.0; however, as reservoir-induced earthquakes are shallow source earthquakes, they can produce much greater intensity on the ground than tectonic earthquakes of the same magnitude (Chen *et al*., 2008). Qin and Qian (2008) found that a reservoir-induced earthquake with the magnitude of 2.0 to 3.0 can produce a seismic magnitude up to V–VI degrees (0.04 g to 0.05 g). Therefore, the reservoir-induced earthquake with a peak acceleration of 0.04 g was considered as the microseism. In the test, the peak acceleration of the natural wave was scaled to 0.04 g. The seismic wave after stitching, compressing and scaling is shown in Fig. 2.

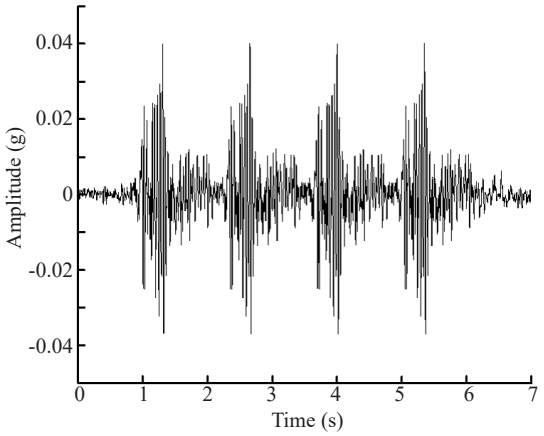

Fig. 2 Waveform of natural seismic wave after stitching, compressing and scaling

Sine wave was adopted as the artificial wave and its amplitude was 0.15 g, 0.2 g and 0.4 g. The 30 s white noise with an amplitude of 0.08 g was used to determine the dynamic characteristic parameters of the slope model. The detailed working conditions of the shaking

table test are summarized in Table 4.

After each loading stage or when the number of loading reached 50 times, the slope model was subject to white noise scanning. There were 29 white noise excitations conducted in the shaking table test. The white noise was denoted successively as WN-1, WN-2, . . ., WN-29.

2.1.3 Test equipment and test process

The test was carried out on a two-way and two-degree-of-freedom earthquake-simulated shaking table. The table is 1.2 m×1.2 m in size and can handle a maximum weight of 1000 kg. The maximum acceleration at full load (1000 kg) is 1.2 g horizontally and vertically. The maximum acceleration at the load of 500 kg is 2.0 g horizontally and vertically. The maximum displacements in the horizontal direction is ±100 mm with a loading frequency range of 0–50 Hz.

The operation process of the vibrating table was as follows: lifting the model slope to the shaking table, connecting and debugging the sensors, implementing test loadings and observing cracks throughout the process, collecting experimental data and recording the failure process. The partial shaking table test procedure is shown in Fig. 3.

2.2 Experimental results and analysis

2.2.1 Dynamic characteristics of the slope

The dynamic characteristics of the slope mainly refers to its natural frequency, damping ratio and the mode of vibration, which determine the response pattern of the slope under dynamic load. Based on the responding signals of the slope model under white noise excitation, MATLAB's estimate function in the Signal Processing Toolbox was used to obtain transfer functions of the model. The transfer functions of WN-1 excitation, calculated from monitoring points A1, A2, A3, A4, and A5 are shown in Fig. 4. The corresponding first-order natural frequency of the slope model was 24.89 Hz, as shown in Fig. 4.

The average value of first-order natural frequency and corresponding damping ratio of the slope model under all conditions of WN were obtained by the transfer functions. The variation rules of these two dynamic parameters with the loading process are shown in Fig. 5.

The curves of the first order natural frequency and damping ratio of slope models with the loading process are shown in Fig. 5. The damping ratios showed an

Table 4 Loading plan of the input seismic waves

Working conditions	Amplitude (g)	Wave type (*X* direction)	Time (s)	Frequency (Hz)	Loading times
1	0.08	White noise 1	30		1
2–51	0.04	Natural wave	7	32	50
52	0.08	White noise 2	30		1
Repeating No. 2-52 loading conditions until to the 511th condition, totally of 500 microseisms					
512–561	0.15	Sine wave	7	30	50
562	0.08	White noise 12	30		1
Repeating No. 512–562 loading conditions until to the 1021st condition, totally of 500 small earthquakes					
After the 1021st condition, loading sinusoidal wave of 0.2–0.4 g with frequency 15 Hz until the slope was destroyed					

Fig. 3 Partial shaking table test procedure

upward trend with the increase in loading times, while the natural frequencies presented a decreased trend. The damping ratios of the slope model were 11.32% before loading and 15.35% after loading, with an increase of 35.6%. By contrast, the natural frequencies were 24.89 Hz before loading and 21.32 Hz after loading, with a decrease of 14.3%. The results showed that the natural frequencies decreased and the damping ratios increased along with the increase in the loading times of earthquakes were the basic variation law of the dynamic parameters of the slope. In addition, the dynamic response of the slope model was different when the input seismic amplitude varied. The variation rate of both natural frequencies and damping ratio were slow when the input seismic amplitude was 0.04 g. The natural frequencies decreased slowly when the input seismic amplitude was 0.04 g. Although the damage to the slope caused by a certain number of the microseisms was not obvious, the cumulative damage increased with the increase in the loading times of microseisms. As the amplitude increased to 0.15 and 0.2-0.4 g, the variation rate of both natural frequencies and damping ratio increased, which indicated that a strong ground motion led to fast and significant damage to the slope.

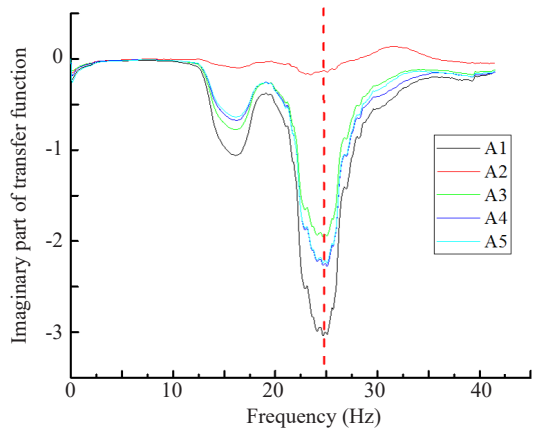

Fig. 4 Imaginary part of the transfer functions in different measuring points under WN-1 condition

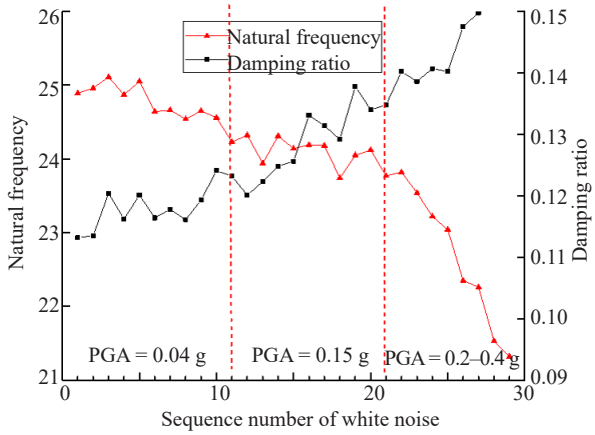

Fig. 5 Curves of the first-order natural frequency and damping ratio of slope model with the loading process

2.2.2 Effects of loading times

The amplification coefficient of PGA was used to describe the acceleration response laws of the model slope in the test. The amplification coefficient of peak ground acceleration here is defined by the ratio of the PGA measured at any monitoring point to that measured at the slope bottom (A1). The relative elevation (h/H) is defined as the ratio of height of any monitoring point (h, measured from the slope bottom) to the total height (H) of the slope. The relative width (b/B) is defined as the ratio of the horizontal distance from the accelerometers to the slope surface (b) to the length of the slope top (B).

Damage continued to accumulate with the increase in loading times. The propagation paths of seismic waves in the slope changed as the initial damage developed, which affected the dynamic response characteristics of the slope. The PGA amplification coefficients of measuring points on the slope surface at the initial stage, the stage of 500 microseisms and the stage of 500 small earthquakes are shown in Fig. 6.

Figure 6 shows that the PGA amplification coefficient of the slope presented a decreasing trend as the loading times of earthquakes increased. This can be explained by the extended cracks in the slope body, and shear cracks on bedding surfaces, which had a significant effect on slope integrity. Part of the seismic energy dissipated during the propagation and coalescence of microcosmic cracks inside the slope, causing the filtering effect of slope to increase gradually as the damage cracks increase. Therefore, the seismic energy of upward propagation decreased as the filtering effect increased gradually. This phenomenon showed that the damage of the slope continued to accumulate under repeated earthquakes.

2.2.3 Failure mode of the model slope

The crack propagation, sliding surface formation and instability failure process of the bedding rock slope under thousands of earthquake loadings are shown in Fig. 7. According to the characteristics of slope deformation and crack propagation observed throughout the shaking table test, the formation of the sliding surface

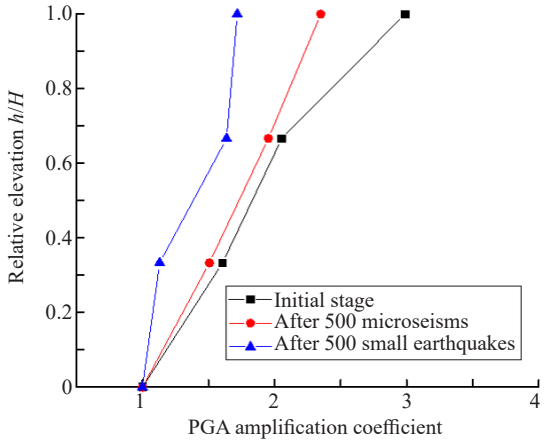

Fig. 6 Variation of PGA amplification coefficient with the number of earthquakes

and instability failure process of the bedding slope were divided into the following stages.

Stage 1: Vertical tensile crack develops at the slope rear edge (as shown in Fig. 7(a)). The bedding plane exposed in the slope surface and the inclination angle of it is relatively large, so the middle and upper rock mass tended to slide down along the bedding plane the under horizontal seismic action. Consequently, large tensile stress occurred at the slope rear edge; thus, the secondary joints of weaker tensile strength cracked first. Vertical tensile cracks expanded gradually from top to bottom, and the cracks finally went through with the bedding plane on the underlying stratum. At this stage, the tensile cracks at the slope rear edge were formed and expanded, and the sliding resistance force of the sliding body was mainly provided by the shear strength of the bedding plane.

Stage 2: Vertical tensile cracks widened and the underlying failure surface gradually formed (as shown in Fig. 7(b)). After the vertical tensile cracks went through, slip deformation of the upper slope rock mass along the bedding plane accumulated as the number of seismic action increased. Due to the increase of the cumulative displacement of the upper slope rock mass, the vertical tensile cracks were widened. The cracks in the lower bedding plane developed towards the slope surface. At the same time, a small amount of dislocation along the plane occurred between the rock layers of the sliding body due to the difference of slip displacement, which made it easier for the strata above the lower lying layer to penetrate into the slope surface.

Stage 3: Slope integral sliding instability (as shown in Fig. 7(c)). Failure surfaces (slide surface 1 and slide surface 2) were formed after the cracks on the bedding plane were linked up with the vertical tensile cracks. When the residual shear strength of the slide surface could not resist the sliding force of the upper strata, integral landslide along the bedding plane would occur.

3 Numerical modelling

The model slope in the shaking table test experienced a total of about 1200 times of seismic action, including 500 microseisms, 500 small earthquakes and about 200 strong earthquakes. It could be seen that strong earthquakes were adopted in the late loading phase due to the testing apparatus and cost restrictions, so the final failure mode of model slope in the shaking table test had the characteristics of the strong earthquake. In addition, it is difficult to acquire the evaluation index of slope stability directly by shake table testing. Consequently, the discrete element method UDEC was adopted to study the dynamic stability evaluation of bedding rock slopes under purely repeated microseisms. This section presents a numerical simulation for the above model test and additional conditions are investigated.

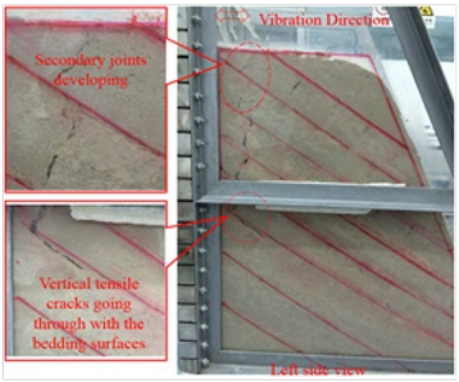

(a) Stage 1

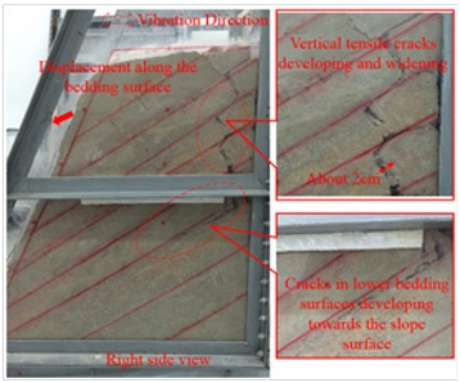

(b) Stage 2

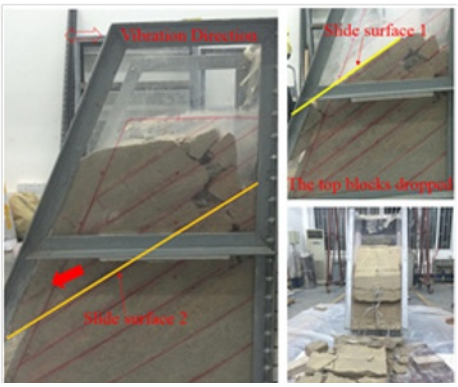

(c) Stage 3

Fig. 7 Sliding surface forming process and failure mode of model slope

3.1 Dynamic formulation in UDEC

3.1.1 Model setup and boundary conditions

More strata inclinations, bedding plane spacing, slope angles and slope heights are considered in the numerical analysis. Four groups of bedding plane dip angles are analyzed, i.e., 0, 15, 30, 60 degrees. Four groups of strata thicknesses are analyzed, i.e., 0.5, 1.0, 1.5, 2.0 m. Four groups of slope angles are analyzed, i.e., 30, 45, 60, 70 degrees. Four groups of slope heights are analyzed, i.e., 19.4, 50, 100, 150 m. See Table 5 for the calculation conditions in the numerical simulation. Calculation condition 3 corresponds to the prototype slope in the shake table testing.

The geometric dimension, boundary conditions and grid division of the slope model in the numerical analysis is shown in Fig. 8. The length of the numerical calculation model is (1.1+cot$a$)H and the height of it is 1.3H. In the model, both lateral sides of the rock slope are considered as the free-field boundary to absorb energy. The base of the slope is considered as the viscous boundary and fixed in the y-direction. Since the local damping and the viscous boundary is independent of frequency, the estimation of the natural frequency of the modeled system is not needed (Luo *et al.*, 2012). As there is no need to specify the frequency, the use of local damping is simpler than Rayleigh damping. Thus, the local damping is adopted in the present analysis. Referring to the user's manual of UDEC (Itasca, 2014), the local damping coefficient can be written as

$$\alpha_{\mathrm{L}} = \pi \mathrm{d} \tag{1}$$

where α_{L} is the local damping coefficient, and d is the damping coefficient and can be set to 0.05. Thus, the local damping with a damping factor of 0.15 is adopted.

The rock material is assumed to be an ideal elastic-plastic model subject to the Mohr-Coulomb yield criterion. The model of bedding planes and the orthogonal secondary joints is chosen as the built-in Coulomb slip model, which is sufficient for most static and dynamic analyses (Itasca, 2014). Linear elastic constitutive relation is adopted for both the free-field boundary and the viscous boundary.

Table 5 Calculation conditions for numerical modeling

No.	Strata inclination β (°)	Bedding plane spacing D (m)	Slope angles a (°)	Slope height H (m)
1	0	2.0	60	19.4
2	15	2.0	60	19.4
3	30	2.0	60	19.4
4	60	2.0	60	19.4
5	30	0.5	60	19.4
6	30	1.0	60	19.4
7	30	1.5	60	19.4
8	30	2.0	30	19.4
9	30	2.0	45	19.4
10	30	2.0	70	19.4
11	30	2.0	60	50
12	30	2.0	60	100
13	30	2.0	60	150

In dynamic analysis, the dimension of the model grid division is dependent on the shortest wave of seismic wave input. Lysmer and Kuhlemeye (1969) suggested that the maximum dimension Δl of a unit should be less than 1/10–1/8 of the minimum wave length. According to elastic wave propagation theory, the P-wave velocity (C_{p}) and S-wave velocity (C_{s}) are calculated as follows:

$$\begin{cases} C_{\mathrm{p}} = \sqrt{\dfrac{K + 4G/3}{\rho}} \\ C_{\mathrm{s}} = \sqrt{\dfrac{G}{\rho}} \end{cases} \tag{2}$$

where G and K are the static shear and bulk modulus of materials, respectively, and ρ is the density of materials.

C_{p} and C_{s} in different rock stratum materials are calculated by Eq. (1). Use f = 25 Hz to control the precision of grids after an overall consideration of the calculation speed and the distribution of proposed seismic wave frequencies. The maximum dimension of a grid Δl is calculated by the following equation:

$$\Delta l = \frac{1}{10} \cdot \frac{C_{\mathrm{s}}}{f} \tag{3}$$

The calculated maximum dimension Δl is 5.5 m and the dimension of the model grid division is chosen to be 1.0 m to improve the accuracy of calculation.

As seen in Fig. 8, the rock blocks are mainly divided into the square blocks with the side length approximately

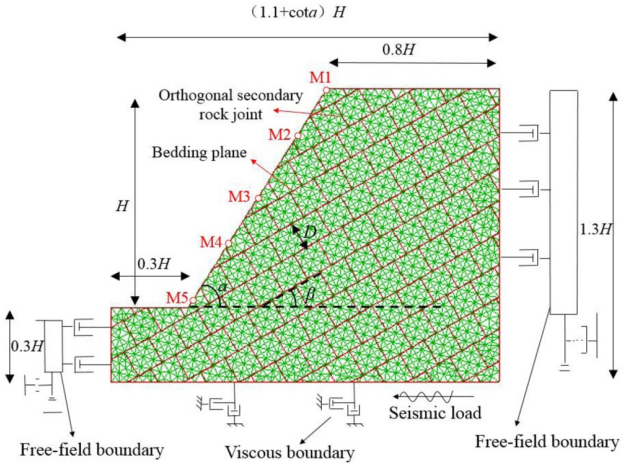

Fig. 8 Mesh division, geometric dimension and boundary condition of numerical analysis model

equal to the thickness of the layer, and the shape of the blocks at the corners is slightly adjusted. The blocks are then divided into a large number of triangular elements.

3.1.2 Parameter selection

Sandstone is used as the model material in the numerical calculation and the physical-mechanical parameters of materials for the prototype slope is adopted for sandstone. Parameters of sandstone and boundaries are listed in Table 6.

For the value of parameters of secondary joints and bedding planes, it is recommended that the values of normal and tangential stiffness should not exceed 10 times the equivalent stiffness of meshes with the highest joint stiffness, which are close to the grid (Itasca, 2014). The expression is:

$$k_{\mathrm{n}}, k_{\mathrm{s}} \leq 10.0\left[\max\left(\frac{K+4G/3}{\Delta Z_{\min}}\right)\right] \tag{4}$$

where k_{n} and k_{s} are the values of normal and tangential stiffness separately.

In addition, the value of normal stiffness should not be too small, and the normal displacement of the joint calculated by it should not be greater than 0.1 times the mesh size close to the joint. The expression is:

$$\frac{10\sigma}{\Delta Z_{\mathrm{adjoining}}} \leq k_{\mathrm{n}} \tag{5}$$

where $Z_{\mathrm{adjoining}}$ is the mesh size close to the joint.

Parameters of bedding planes and secondary joints are listed in Table 7.

3.1.3 Input loading

The sinusoidal shear wave with an amplitude of 0.04 g and a holding time of 7 s is selected as the input seismic wave. The expression of the acceleration time-history curve is:

$$a = \lambda \sin(2\pi f t) \tag{6}$$

where a is the acceleration, λ is the amplitude with a value of 0.04 g, f is frequency and t is time.

The input loads are applied to the base of the model with viscous boundary conditions, while the input acceleration wave cannot be directly applied to the viscous boundary in UDEC. Consequently, the input acceleration wave should be first integrated numerically to produce the velocity history, then converted into a stress record, before being applied to the viscous boundary. The expression for conversion of the velocity time-history into the stress time-history is:

$$\begin{cases} \sigma_{\mathrm{n}} = 2(\rho C_{\mathrm{P}})V_{\mathrm{n}} \\ \sigma_{\mathrm{s}} = 2(\rho C_{\mathrm{S}})V_{\mathrm{s}} \end{cases} \tag{7}$$

where σ_{n} and σ_{s} are the normal and shear stress, respectively, and v_{n} and v_{s} are input velocities in vertical and horizontal directions, respectively.

Convert Eq. (2) into Eq. (7), the expression for the stress time-history is:

$$\sigma_{\mathrm{s}} = \frac{\mathrm{g}t}{2\pi}\sqrt{\frac{E\rho}{2(1+\upsilon)}}\sin\left(\frac{2\pi}{T}t\right) \tag{8}$$

3.2 Dynamic strength reduction method

The dynamic response analysis of the slope under the seismic excitations is conducted with the gradual reduction of the strength parameters of rock mass and structural plane using the dynamic strength reduction method. The trail reduction factor k is first adopted as a lower value and then gradually increased to a higher value until the computational model enters an unbalanced state. The reduction factor k is then defined as the slope safety factor. The following reduction formula is used in this study:

$$c' = \frac{c}{k},\ \varphi' = \arctan\left(\frac{\tan\varphi}{k}\right),\ \sigma_{\mathrm{t}}' = \frac{\sigma_{\mathrm{t}}}{k} \tag{9}$$

where c, φ, and σ_{t} are, respectively, the cohesion, internal

Table 6 Parameters of sandstone and boundaries

Category	Density ($\mathrm{g\cdot cm^{-3}}$)	Elastic modulus (MPa)	Poisson ratio (μ)	Cohesion (kPa)	Internal friction angle (°)	Tensile strength (MPa)
Sandstone	2.50	5868	0.25	2736	42	2
Free-field boundary and viscous boundary	2.50	5868	0.25	-	-	-

Table 7 Parameters of bedding plane and secondary joint

Category	Cohesion (kPa)	Tensile strength (kPa)	Internal friction angle (°)	Normal stiffness ($\mathrm{GPa\cdot m^{-1}}$)	Tangential stiffness ($\mathrm{GPa\cdot m^{-1}}$)
Bedding plane	30	80	32	10.2	6.4
Secondary joint	6	3	20	8.2	5.1

friction angle and tensile strength of slope rock in the initial state; c', φ', and σ_t' are, respectively, the cohesion, internal friction angle and tensile strength of slope rock after reduction; and k is the reduction coefficient.

As a type of search algorithm, the dynamic strength reduction method determines the critical failure state of the slope through constantly adjusting the reduction factor. Therefore, judging the instability state of the slope is the key problem in the dynamic strength reduction method. The judgment method whether the numerical calculation is convergent is adopted. When the ratio between the maximum unbalanced mechanical force magnitude for all block centroids or gridpoints in the model and the average applied mechanical force magnitude for all the block centroids or gridpoints is greater than a certain allowable value, the computational model is considered to be in an instability state; otherwise, the numerical calculation is considered to be convergent. In this study, the allowable value is 10^{-5}.

3.3 Analysis of results of influencing factors

See Figs. 9(a)-9(e) for the influencing factors of seismic amplitude, slope height, slope angle, strata inclination and strata thickness on the variation rules between the stability coefficient and the loading times. From Figs. 9(a)-9(e), the safety factor of the slope under frequent microseisms generally presented the trend of decreasing slowly to quickly as the microseism loading times increase. And when the microseism increases to a certain number of times, the safety factor of the slope decreased sharply to less than 1, which indicated that failure of the slope occurred. Simultaneously, the number of microseismic excitations was recorded and defined as the fatigue life of the slope; thus, the relationship between the long-term stability of the slope and the number of microseismic excitations was established. Therefore, the number of microseismic excitations before the slope failure was applied as an

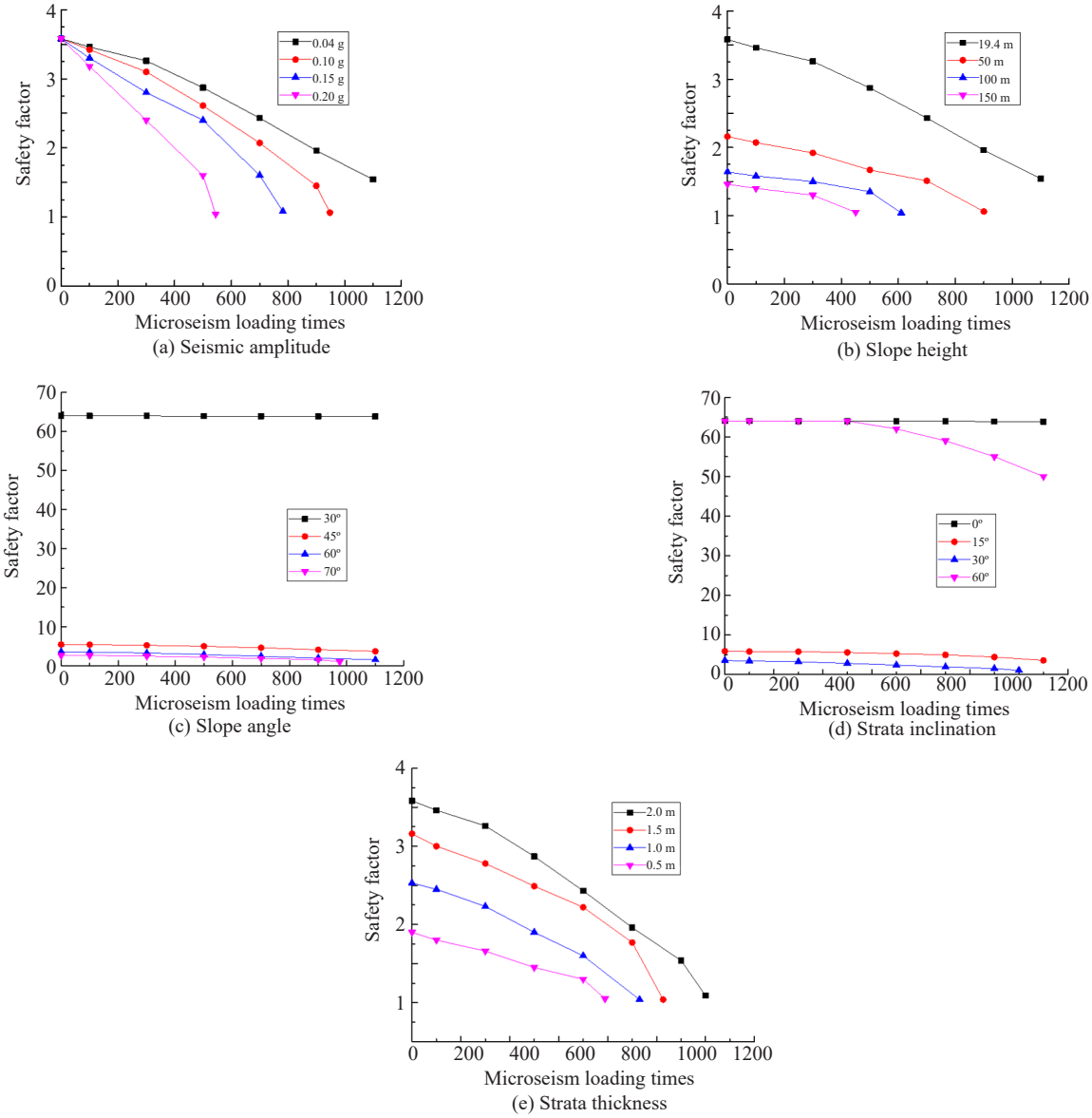

Fig. 9 Relationship between the stability coefficient and the loading times

index to consider the long-term stability of a slope. And the more microseismic excitations the slope experienced before failure, the better the slope's long-term stability.

In order to study the influence of seismic amplitude on the stability of the bedding rock slope, four groups of sinusoidal shear waves with seismic amplitude of 0.04 g, 0.10 g, 0.15 g, 0.20 g, respectively, were applied on the prototype slope (β = 30°, D = 2.3 m, a = 60°, H = 22.9 m). See Fig. 9(a) for the stability coefficient of the slope based on numerical analysis. According to Fig. 19(a), with the increase of loading times, the stability coefficient of the slope decreased gradually and the stability coefficient presented the law of decreasing linearly at first and suddenly dropping sharply to less than 1. The mutation of the stability coefficient of the slope indicated that it was in a critical state of instability. In addition, the safety factor of the slope decreased with the increase of seismic amplitude. The seismic loading times when the slope was in a critical state of instability with seismic amplitudes of 0.04 g, 0.10 g, 0.15 g, 0.20 g were 1194 times, 948 times, 782 times and 545 times, respectively, which showed that the greater the seismic load amplitude, the faster the safety coefficient of slope decreased, the more the accumulated damage of slope body and the weaker the slope safety.

Take four groups of model slope (β = 30°, D = 2.3 m, a = 60°) with the slope height H = 22.9 m, 50 m, 100 m, 150 m, respectively, for a dynamic numerical calculation. The variation curve of the stability coefficient to the seismic loading times of different slope heights is shown in Fig. 9(b). According to Fig. 9(b), the higher the slope, the smaller the corresponding stability coefficient and the worse the slope stability under the same loading times. Under the condition of the same loading times, the sliding force of the slope increases as the slope height increases, while the anti-sliding force does not change because the strength of slope body and slope structure surface remains the same. Therefore, the slope stability will be reduced as the slope height increase. The seismic loading times when the slope was in a critical state of instability with slope heights of 22.9 m, 50 m, 100 m, 150 m were 1194 times, 903 times, 612 times and 447 times. Therefore, frequent microseisms can also cause a significant effect on the slope stability, especially when the slope height is more than 150 m.

Take four groups of model slope (H = 22.9 m, β = 30°, D = 2.3 m) with the slope angles of a = 30°, 45°, 60°, 70°, respectively, for a dynamic numerical calculation. The variation curve of the stability coefficient to the seismic loading times of different slope angles is shown in Fig. 9(c). As seen in Fig. 9(c), as the bedding surfaces are not exposed in the slope surface when the slope angle is 30°, which is equal to the strata inclination, the stability coefficient of the slope is stable and over 64 within 2000 loading times. As the slope angle increases, the bedding surfaces are exposed in the slope surface, and the corresponding stability coefficient of the slope gradually decreases. This variation law of slope stability coefficient and its cause is similar to that of the slope height.

Take four groups of model slope (H=22.9 m, D=2.3 m, a=60°) with the strata inclinations of β=0, 15°, 30°, 60°, respectively, for a dynamic numerical calculation. The variation curve of the stability coefficient to the seismic loading times of different strata inclinations is shown in Fig. 9(d). From Fig. 9(d), when the strata inclination is 60°, the slope is very stable within 2000 loading times with the high stability coefficient as the bedding surfaces are not exposed in the slope surface. However, when the bedding surfaces are exposed in the slope surface, the initial stability coefficient decreases from 64.00 to 5.92 to 3.58 as the strata inclination increases from 0 to 15° to 30°. The slope stability coefficient decreases by 90.75% when the strata inclination increases from 0 to 15°, while it decreases by 94.41% when the strata inclination increases from 0 to 30°. It can be concluded that the horizontal bedding slope has extremely good stability under the frequent microseisms, while the slight increase in the strata inclination makes the stability coefficient of the slope sharply decrease.

Take four groups of model slope (H=22.9 m, β=30°, a=60°) with the strata thicknesses of D=2.3 m, 1.5 m, 1.0 m, 0.5 m, respectively, for a dynamic numerical calculation. The variation curve of the stability coefficient to the seismic loading times of different strata thicknesses is shown in Fig. 9(e). As seen in Fig. 9(e), the stability coefficient of the slope increases with the increase of strata thicknesses. The seismic loading times when the slope was in a critical state of instability with strata thicknesses of 2.3 m, 1.5 m, 1.0 m, 0.5 m were 1194 times, 1027 times, 934 times and 789 times. This is related to the complex wave field formed by the reflection and refraction of the vibration stress wave leading to damage of the internal structure when the vibration stress wave spreads to the bedding planes. And the more bedding surfaces, the greater the damage to the internal structure. When the slope size and shape is determined in the numerical simulation, there will be fewer bedding surfaces with higher strata thickness; and on the contrary, more bedding surfaces with lower strata thickness. Therefore, the slope is more likely to lose stability with the lower strata thicknesses.

4 Discussion

4.1 Differences in failure modes of the model slope in shaking table test and the numerical simulation

The models of the shake table testing and from the numerical simulation test are the same in terms of geometry, lithology and structure. However, the model of the shaking table test experienced about 1200 times of seismic action, including microseisms, small earthquakes and strong earthquakes due to the testing apparatus and cost restrictions, while the model of the

numerical simulation test only experienced microseismic excitation in order to further study the dynamic stability of the bedding rock slope under frequent microseisms. Based on the failure phenomenon of the model slope observed in the shaking table test, the formation and destabilization evolution of the slide surfaces are shown in Fig.10(a), while the fatigue failure process of slope under repeated microseisms in the numerical simulation is shown in Fig.10(b), which was recorded as the seismic action times increased until the slope failed.

As shown in Fig. 10(a), in the shaking table test, the sliding surfaces of the slope was composed of the

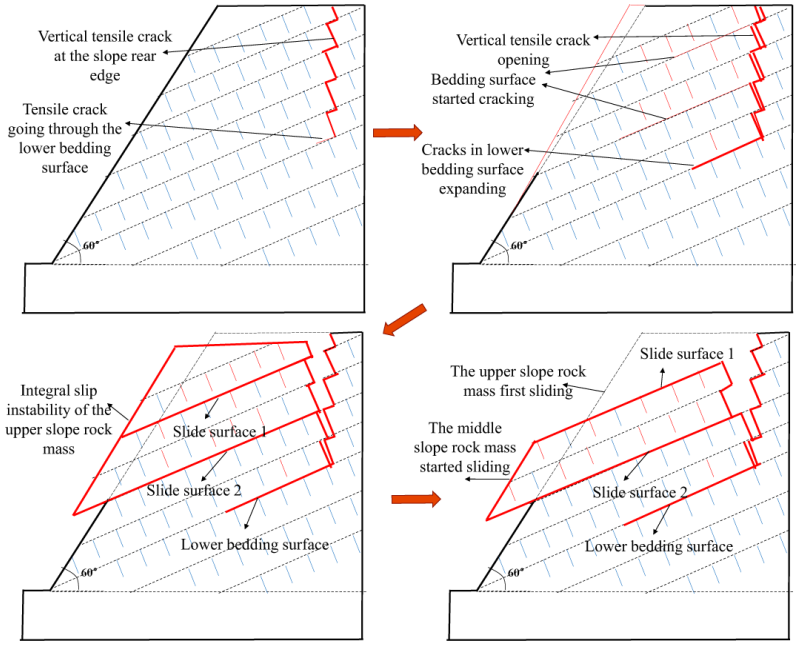

(a) Shaking table test

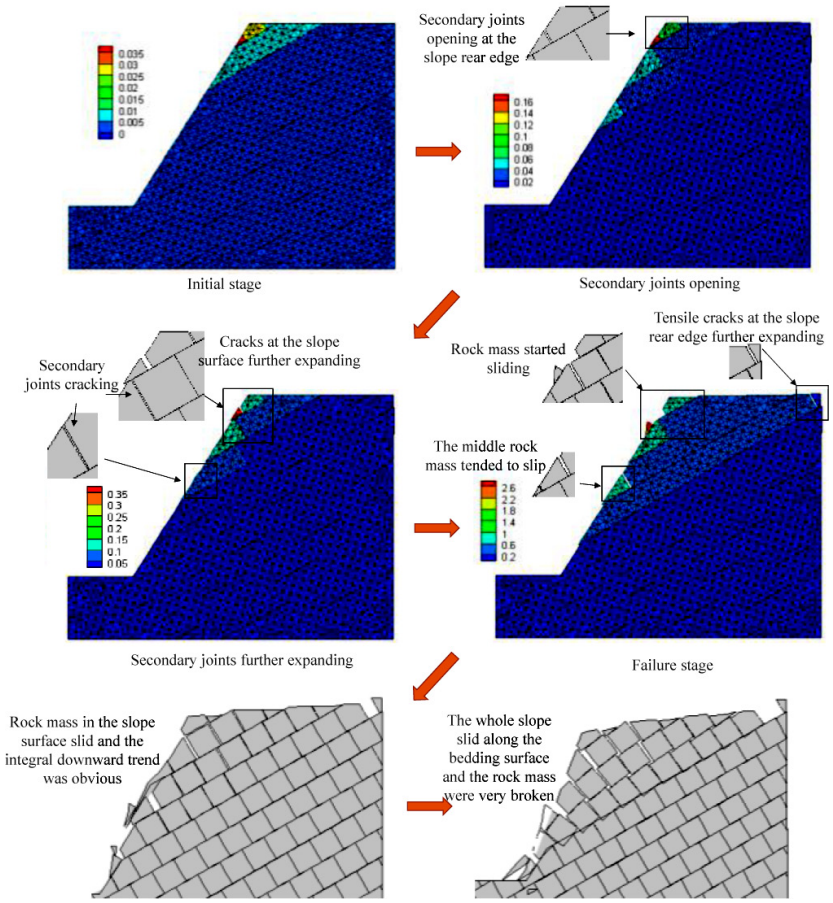

(b) Numerical simulation (mid-dip bedding slope (β = 30°))

Fig. 10 Fatigue failure process of shaking table test and the numerical simulation

vertical tensile crack at the slope rear edge and cracks on the bedding surface, the sliding blocks with the integral slipping instability were divided into two parts falling off the slope. Two sliding surfaces were formed under frequent microseism actions. The failure mode of the bedding rock slope can be summarized as follows: opening tensile cracks at the slope rear edge—developing cracks along the bedding surface and in the sliding block—forming sliding surface 1 and the upper sliding block falling off—forming sliding surface 2 and the medium sliding block falling off. By contrast, in the numerical simulation, the dipping tensile cracks, which was apparent in the shaking table test, did not occur at the slope rear edge. Moreover, the sliding block had become very broken before it fell off the slope. The difference in failure modes between the shaking table test and the numerical simulation can be explained by the fact that small earthquakes and strong earthquakes were adopted in the late loading stage in the shaking table test, while purely microseisms were adopted in the numerical simulation. Before the sliding block slipped along the bedding surfaces, the secondary joints in the rock stratum were pulled apart, and they were completely pulled apart due to the slippage of the rock strata that slowly developed layer by layer under purely microseism actions, so the sliding blocks were more broken in the numerical simulation than in the shaking table test. However, despite these differences, the shaking table test and the numerical simulation both showed that the failure mode of a mid-dip bedding slope (β = 30°) were integral slipping along the bedding surface.

4.2 Failure mode of the model slope in numerical simulation

Figures 11(a) and 11(b) show the fatigue failure process of the model slope (H=22.9 m, D=2.3 m, a=60°) with different strata inclination (β = 0°, 60°) under

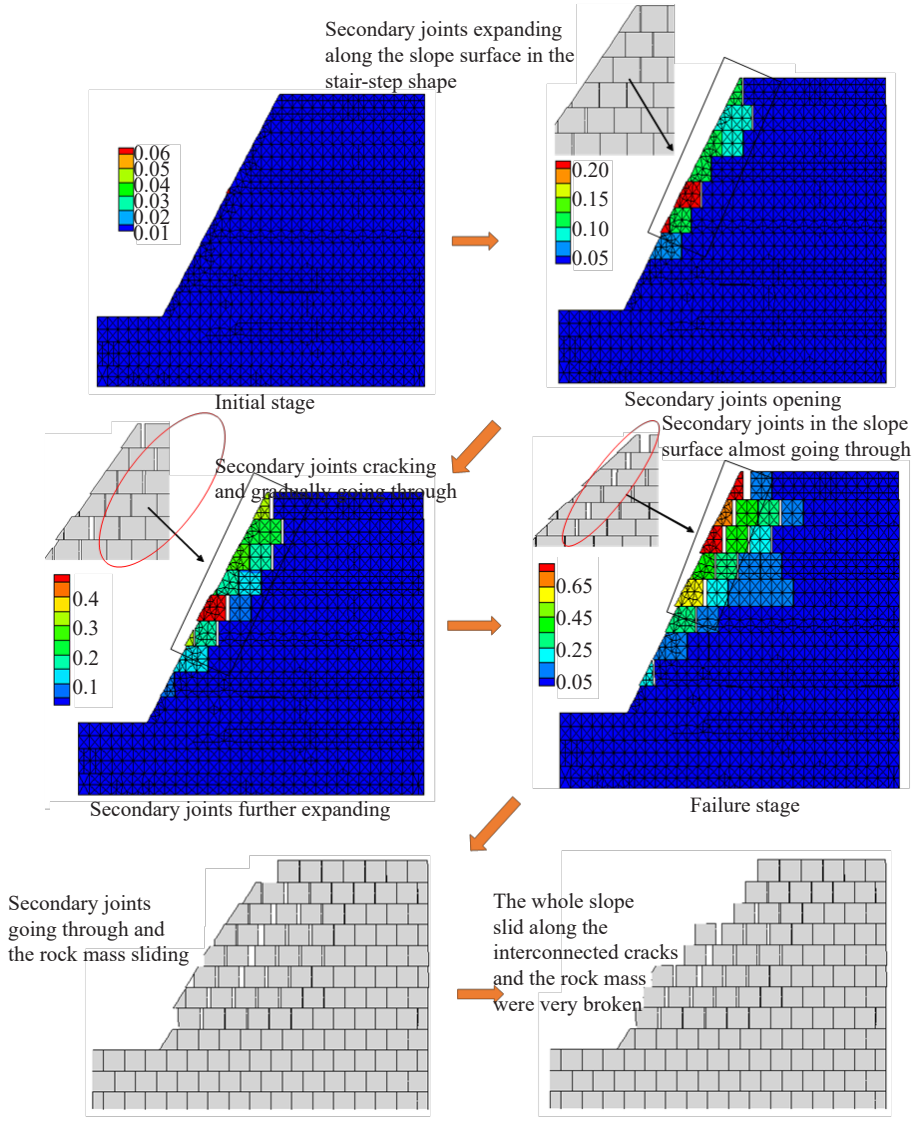

(a) Horizontal bedding slope (β = 0°)

Fig. 11 Fatigue failure process of the numerical simulation

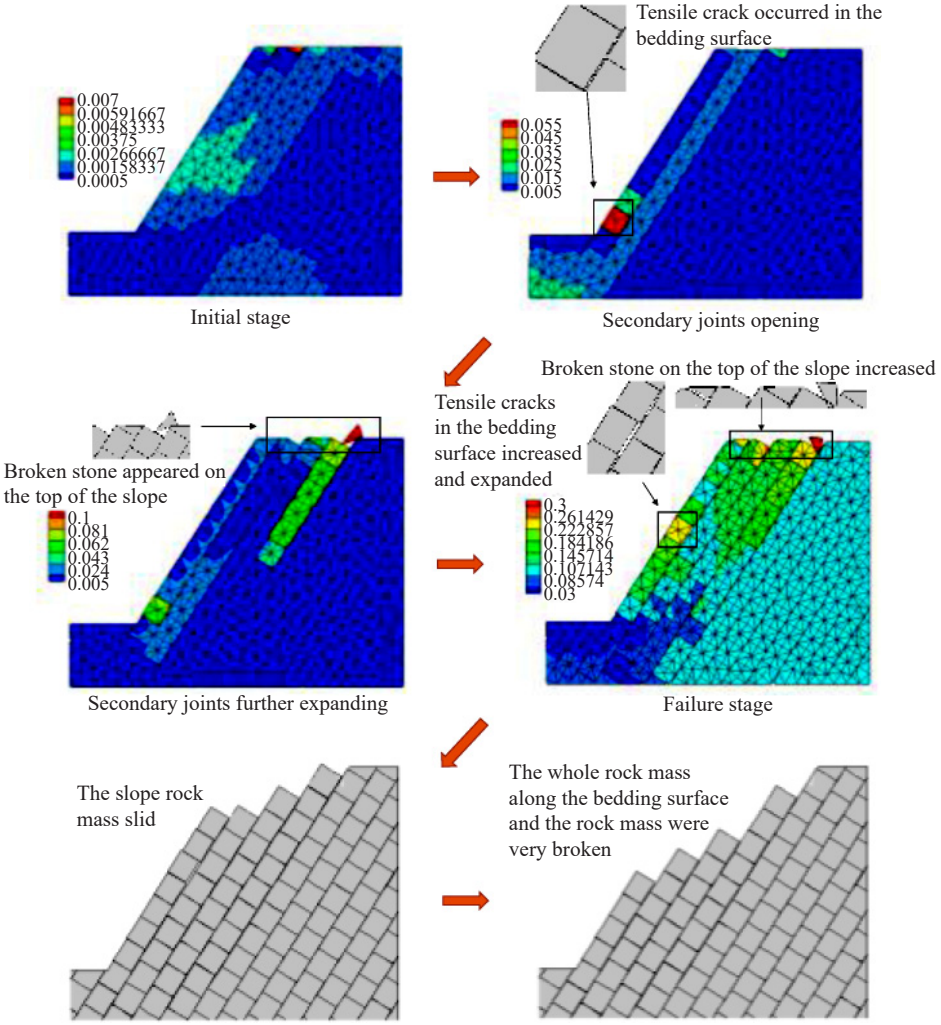

(b) Steep bedding slope (β = 60°)

Fig. 11 Continued

repeated microseisms. Combined with the fatigue failure process of the model slope with a strata inclination of 45° shown in Fig. 10(b), it shows that the stability of the mid-dip bedding slope (β = 30°), the bedding surfaces of which is exposed in the slope surface and inclined, is the worst. The slope began to show signs of slip instability after about 1200 microseisms. For the steep bedding slope (β = 60°), the bedding surfaces of which are exposed in the slope surface, the signs of slip instability occur after about 3000 microseisms and its stability is better than that of the mid-dip bedding slope. The stability of the horizontal bedding slope (β = 0) is the best among them, the signs of slip instability occur after about 8000 microseisms, and the slope failure is mainly due to the large horizontal displacement of rocks near the slope surface causing the partial slope structure to become loose and collapse. Combined with the integral slipping of the mid-dip bedding slope, the failure mode of the horizontal bedding slope can be summarized as local instability.

It was found that the long-term stability of the mid-dip bedding slope was the worst under frequent microseisms and the slope has the integral sliding instability risk. Obvious signs of deformation development and very broken slipping mass can be observed before the integral slipping of the slope. The stability of the steep bedding slope is better than that of the mid-dip bedding slope, and the slope failure is mainly caused by geological disasters such as collapse and rockfall. Frequent microseisms have little influence on the stability of the horizontal bedding slope, but after a long period of microseisms, the rocks near the slope surface are relatively broken, and there is a risk of local rocks falling off and local instability.

5 Conclusion

Shake table testing was performed to investigate the dynamic response and failure mode of the bedding rock slope under frequent earthquakes. Numerical modelling was then performed to further study the slope dynamic stability under purely microseisms and the influence of five factors, including seismic amplitude, slope height, slope angle, strata inclination and strata thickness, on

the dynamic stability was considered. The results of the shaking table test and the numerical simulation were compared and analyzed. The following conclusions were obtained:

(1) With the increase of loading times of the earthquakes, natural frequencies presented a downward trend and damping ratios showed an upward trend. Therefore, the basic variation law of its dynamic characteristics is characterized by the decrease of the natural frequency and increase of the damping ratio of the slope.

(2) The slope stability decreased with the increase of seismic amplitude, increase of slope height, reduction of strata thickness and increase of slope angle. In addition, the safety factor of the slope under frequent microseisms decreased sharply when the microseismic excitations increased to certain loading times, which indicated that the instability of the bedding rock slope under frequent microseisms had the characteristic of a certain degree of mutation.

(3) The dynamic failure mode of the mid-dip bedding rock slope is mainly characterized by vertical tensile cracks at the slope rear edge and integral slipping of the slope along the bedding surfaces. By contrast, in the numerical simulation, the failure mode of the mid-dip bedding rock slope is also integral slipping along the bedding surface, whereas slope rock mass is very broken and dipping tensile cracks do not occur at the slope rear edge.

(4) Under frequent microseisms, the long-term stability of the mid-dip bedding slope is the worst and the horizontal bedding slope is best. The slope failure of the steep bedding slope is mainly caused by geological disasters such as collapse and rockfall, while the slope failure of the horizontal bedding slope is mainly caused by local rocks falling off and local instability after it experienced a long period of microseisms.

Acknowledgement

The authors acknowledge the financial support provided by the National Natural Science Foundation of China (No. 41372356), the Basic Research and Frontier Exploration Project of Chongqing, China (cstc2018jcyjA1597), the College Cultivation Project of the National Natural Science Foundation of China (No. 2018PY30) and the Graduate Scientific Research and Innovation Foundation of Chongqing, China (No. CYS18026).

References

Almaz T and Havenith HB (2016), "2D Dynamic Studies Combined with the Surface Curvature Analysis to Predict Arias Intensity Amplification," *Journal of Seismology*, **20**(3): 711–731.

Aurelian CT, Toshitaka K and Roy CS (2009), "Earthquake-Induced Displacements of Gravity Retaining Walls and Anchor-Reinforced Slopes," *Soil Dynamics and Earthquake Engineering*, **29**(3): 428–437.

Aydan Ö, Ohta Y, Geniş M, Tokashiki N and Ohkubo K (2010), "Response and Stability of Underground Structures in Rock Mass during Earthquakes," *Rock Mechanics and Rock Engineering*, **43**(6): 857–875.

Barbero M and Barla G (2010), "Stability Analysis of a Rock Column in Seismic Conditions," *Rock Mechanics and Rock Engineering*, **43**(6): 845–855.

Bhasin R and Kaynia AM (2004), "Static and Dynamic Simulation of a 700-m High Rock Slope in Western Norway," *Engineering Geology*, **71**(3): 213–226.

Chen D, Wang Y and Zeng X (2008), "A Study of Reservoir-Induced Earthquake of Three Gorges Project," *Chinese Journal of Rock Mechanics and Engineering*, **27**(8): 1513–1524.

Chen Z, Hu X and Xu Q (2016), "Experimental Study of Motion Characteristics of Rock Slopes with Weak Intercalation under Seismic Excitation," *Journal of Mountain Science*, **13**(3): 546–556.

Deng Z, Liu X, Liu Y, Liu S, Han Y, Tu Y, and Gu J (2020), "Cumulative Damage Evolution and Failure Modes of the Bedding Rock Slope Under Frequent Microseisms," *Arabian Journal of Geosciences*, **13**(10).

Dong J, Yang J, Wu F, Wang D and Yang G (2010), "Research on Collapse of High Cutting Slope with Horizontal Soft-Hard Alternant Strata in Three Gorges Reservoir Area," *Rock and Soil Mechanics*, **31**(1): 151–157.

Fan G, Zhang J, Wu J and Yan K (2016), "Dynamic Response and Dynamic Failure Mode of a Weak Intercalated Rock Slope Using a Shaking Table," *Rock Mechanics and Rock Engineering*, **49**(8): 3243–3256.

Gibson MD, Wartman JP, MacLaughlin MM and Keefer DK (2018), "Pseudo-Static Failure Modes and Yield Accelerations in Rock Slopes," *International Journal of Rock Mechanics and Mining Sciences*, **102**: 1–14.

Huang J, Zhao M, Xu C, Du X, Jin L and Zhao X (2018), "Seismic Stability of Jointed Rock Slopes Under Obliquely Incident Earthquake Waves," *Earthquake Engineering and Engineering Vibration*, **17**(3): 527–539.

Itasca Consulting Group Inc (2014), "UDEC (Universal Distinct Element Code), Version 6.00," *Software*, Minneapolis, USA.

Jiang J (2012), "Research on the Deformation Mechanism and Dynamic Response of Typical Landslides in Three Gorges Reservoir in Case of Frequent Microseisms," *Dissertation*, China University of Geosciences. (in Chinese)

Koukouvelas I, Litoseliti A, Nikolakopoulos K and Zygouri V (2015), "Earthquake Triggered Rock Falls and Their Role in the Development of a Rock Slope: the Case of Skolis Mountain, Greece," *Engineering*

Geology, **191**: 71–85.

Kundu J, Sarkar K and Singh TN (2017), "Static and Dynamic Analysis of Rock Slope – A Case Study," *Procedia Engineering*, **191**: 744–749.

Kveldsvik V, Kaynia AM, Nadim F, Bhasin R, Nilsen B and Einstein HH (2009), "Dynamic Distinct-Element Analysis of the 800m High Åknes Rock Slope," *International Journal of Rock Mechanics and Mining Sciences*, **46**(4): 686–698.

Lak M, Baghbanan A and Hashemolhoseini H (2017), "Effect of Seismic Waves on the Hydro-Mechanical Properties of Fractured Rock Masses," *Earthquake Engineering and Engineering Vibration*, **16**(3): 525–536.

Li D, Liu X, Li X and Liu Y (2016), "The Impact of Microearthquakes Induced by Reservoir Water Level Rise on Stability of Rock Slope," *Shock and Vibration*, **2016**(2): 1–13.

Li L, Ju N, Zhang S and Deng X (2017), "Shaking Table Test to Assess Seismic Response Differences Between Steep Bedding and Toppling Rock Slopes," *Bulletin of Engineering Geology and the Environment*, **29**(3): 1–9.

Li Y and Huang G (2008), "Some Thoughts on Reservoir-induced Earthquakes," *Technology for Earthquake Disaster Prevention*, **3**(1): 61–71. (in Chinese)

Lin Y, Zhu D, Deng Q and He Q (2012), "Collapse Analysis of Jointed Rock Slope Based on UDEC Software and Practical Seismic Load," *Procedia Engineering*, **31**: 441–446.

Liu H, Xu Q and Fan X (2012), "Influence of Ground Motion Intensity on Dynamic Response Laws of Slope Accelerations," *Rock and Soil Mechanics*, **33**(5): 1357–1365. (in Chinese)

Liu H, Xu Q and Xu H (2011), "Shaking Table Model Test on Slope Dynamic Deformation and Failure," *Rock and Soil Mechanics*, **32**(s2): 334–339. (in Chinese)

Liu H, Xu Q and Li Y (2014), "Effect of Lithology and Structure on Seismic Response of Steep Slope in a Shaking Table Test," *Journal of Mountain Science*, **11**(2): 371–383.

Liu Q, Wu Z and Lee V W (2019), "Scattering and Reflection of SH Waves Around a Slope on an Elastic Wedged Space," *Earthquake Engineering and Engineering Vibration*, **18**(2): 255–266.

Liu X, Han Y, Li D, Tu Y, Deng Z, Yu C and Wu X (2019), "Anti-Pull Mechanisms and Weak Interlayer Parameter Sensitivity Analysis of Tunnel-Type Anchorages in Soft Rock with Underlying Weak Interlayers," *Engineering Geology*, **253**: 123–136.

Liu X, He C, Liu S, Liu Y, Lu Y and Liu Z (2018a), "Dynamic Response and Failure Mode of Slopes with Horizontal Soft and Hard Interbeddings Under Frequent Microseisms," *Arabian Journal for Science and Engineering*, doi:10.1007/s13369-018-3143-0.

Liu X, Liu Y, He C and Li X (2018b), "Dynamic Stability Analysis of the Bedding Rock Slope Considering the Vibration Deterioration Effect of the Structural Plane," *Bulletin of Engineering Geology and the Environment*, **77**(1): 87–103.

Liu X, Liu Y, Lu Y, Li X and Li P (2017), "Numerical Analysis of Evaluation Methods and Influencing Factors for Dynamic Stability of Bedding Rock Slope," *Journal of Vibroengineering*, **19**(3): 1937–1961.

Liu Y, Li H, Xiao K, Li J, Xia X and Liu B (2014), "Seismic Stability Analysis of a Layered Rock Slope," *Computers and Geotechnics*, **55**: 474–481.

Liu Y, Li H, Zhao J, Li J and Zhou Q (2004), "Udec Simulation for Dynamic Response of a Rock Slope Subject to Explosions," *International Journal of Rock Mechanics and Mining Sciences*, **41**: 599–604.

Luo G, Hu X, Gu C and Wang Y (2012), "Numerical Simulations of Kinetic Formation Mechanism of Tangjiashan Landslide," *Journal of Rock Mechanics and Geotechnical Engineering*, **4**(2): 149–159.

Lysmer J and Kuhlemeyer RL (1969), "Finite Dynamic Model for Infinite Media," *Journal of the Engineering Mechanics Division*, **95**: 859–878.

Napier JAL and Peirce AP (1997), "The Use of a Multipole Expansion Technique to Analyze Large Scale Fracture Processes and Seismic Recurrence Effects in Deep Level Mines," *International Journal of Rock Mechanics and Mining Sciences*, **34**(3/4): 680–691.

Pal S, Kaynia AM, Bhasin RK and Paul DK (2012), "Earthquake Stability Analysis of Rock Slopes: a Case Study," *Rock Mechanics and Rock Engineering*, **45**(2): 205–215.

Qin J and Qian X (2008), "The Relation Between Acceleration and Intensity of Reservoir Induced Earthquake," *Seismological and Geomagnetic Observation and Research*, **29**(3): 1–9.

Song D, Che A, Zhu R and Ge X (2018), "Dynamic Response Characteristics of a Rock Slope with Discontinuous Joints under the Combined Action of Earthquakes and Rapid Water Drawdown," *Landslides*, **15**(6): 1109–1125.

Sun G, Yang Y, Jiang W and Zheng H (2017), "Effects of an Increase in Reservoir Drawdown Rate on Bank Slope Stability: A case Study at the Three Gorges Reservoir, China," *Engineering Geology*, **221**: 61–69.

Tang C, Zhu J and Liang J (2009), "Emergency Assessment of Seismic Landslide Susceptibility: a Case Study of the 2008 Wenchuan Earthquake Affected Area," *Earthquake Engineering and Engineering Vibration*, **8** (2): 207–217.

Tang L, Cong S, Ling X and Ju N (2017), "The boundary conditions for Simulations of a Shake-Table Experiment on the Seismic Response of 3D Slope," *Earthquake Engineering and Engineering Vibration*, **16**(1): 23–32.

Xiong M and Huang Y (2017), "Stochastic Seismic Response and Dynamic Reliability Analysis of Slopes: A

Review," *Soil Dynamics and Earthquake Engineering*, **100**: 458–464.

Yang G, Ye H and Wu F (2012), "Shaking Table Model Test on Dynamic Response Characteristics and Failure Mechanism of Anti-Dip Layered Rock Slope," *Chinese Journal of Geotechnical Engineering*, **31**(11): 2214–2221.

Yang JL (2014), "Study on Rock and Soil Mechanics Parameters Partition of Landslides in the Three Gorges Reservoir," *Dissertation*, Chongqing Jiaotong University. (in Chinese)

Yang T, Xu T, Liu H, Zhang C, Wang S, Rui Y and Shen L (2014), "Rheological Characteristics of Weak Rock Mass and Effects on the Long-Term Stability of Slopes," *Rock Mechanics and Rock Engineering*, **47**: 2253–2263.

Zaei ME and Rao KS (2017), "Evaluating the Effect of Strong Earthquake on Slope Instability," *Procedia Engineering*, **173**: 1771–1778.

Zhang B, Yang C, McVerry GH (2010), "Earthquake-Induced Landslide Displacement Attenuation Models and Application in Probabilistic Seismic Landslide Displacement Analysis," *Earthquake Engineering and Engineering Vibration*, **9**(2): 177–187.